

Electrochemical Studies of Nanocrystalline Mg₂Si Thin Film Electrodes Prepared by Pulsed Laser Deposition

Seung-Wan Song,^{a,*} Kathryn A. Striebel,^{a,z,*} Ronald P. Reade,^a
Gregory A. Roberts^b and Elton J. Cairns^{a,b,**}

^aEnvironmental Energy Technologies Division

Ernest Orlando Lawrence Berkeley National Laboratory,

*^bDepartment of Chemical Engineering, University of California,
Berkeley, California 94720, USA*

Abstract

Electrochemically active thin films of Mg₂Si in various film thickness of 30 ~ 380 nm have been prepared with the pulsed laser deposition technique. The thinnest films of 30 nm showed a highly stable cycling behavior at 0.1 ~ 1.0 V vs Li, delivering capacity greater than 2000 mAh/g for more than 100 cycles. Though the film morphology became remarkably rougher with cycling, the films showed good stability. However, the first cycle irreversible capacity loss increased with film thickness. Therefore, lithium adsorption-desorption reaction forming Li-Si alloy at the Si-rich film surface is suggested as one of the sources of the large capacity of the 30 nm film. The superior capacity retention, when compared to porous electrodes of this alloy, may be attributed to a limited structural volume change in the 2-dimensional film, shorter lithium diffusion path and enhanced conductivity from stainless steel substrate. The goals of this study are to help devote toward emerging need of thin film anodes for all solid-state microbatteries and clarify the capacity failure of powder intermetallic anodes for rechargeable lithium batteries.

^zAuthors to whom all correspondence should be addressed.

phone) +1-510-486-4385

fax) +1-510-486-7303

email) kastriebel@lbl.gov

* Electrochemical Society Active Member.

** Electrochemical Society Fellow.

Introduction

The search for anode materials to replace graphite in rechargeable lithium batteries has intensified over recent years due to concerns about safety during overcharge in the presence of organic electrolyte and a highly oxidizing cathode material such as LiCoO_2 .¹ Considerable effort has been devoted to searching for suitable alternative anodes among lithium binary alloys²⁻⁴ and intermetallics⁵⁻¹⁰ which operate a few hundred millivolts above metallic lithium. Magnesium silicide alloys have been studied for this application because Si has a good affinity for lithium.¹¹⁻¹⁶ Consensus regarding the electrochemical reaction between Li and Mg_2Si has not been reached. Part of the reason may be due to the fact that Mg_2Si is a semiconductor whose performance will be dependent on particle morphology and current density, and porous electrodes from alloyed powders show rapid capacity fade over the first ten cycles. It has been generally recognized that lithiation of the alloying metal elements takes place by significant volume change causing electrochemical-mechanical disintegration of particles during cycling.³⁻¹⁵ Many attempts have been made to improve the electrochemical performance of the alloy anode materials by means of controlling the crystal structure to achieve a small lattice volume change and a particle morphology subject to a minimum mechanical stress, based on the study of capacity failure mechanisms of those alloy anodes.¹⁷⁻²⁰ Much can be learned regarding the performance of low conductivity materials when they are in thin film form.^{16,21-23} Thin film electrodes comprise a “pure” material and simpler system; there are no complications from amorphous carbon and binders which are necessary in powder-based porous electrodes. A thin film on an electronically conductive substrate represents a geometry that overcomes many of the uncertainties in the fundamental studies of powder intermetallic anodes, and is also great of interest for lithium microbatteries. Earlier work on thin film anodes as part of the fabrication of an all solid-state lithium battery has been performed with SnO_2 thin films.^{24,25} It has been reported that nanometer scaled anode materials have higher capacity retention, and much larger capacity than any other conventional ones, as they can keep a rather stable and flexible microstructure on structural/mechanical variation and serve uniform dispersion of *in-situ* produced intermediate components at an atomic or nanometer scale during cycling.²⁶⁻²⁹ In this work, we describe the preparation and characterization of thin films of Mg_2Si anode on stainless steel (SS) substrates. The electrochemical behavior is reported as a function of film thickness.

Experimental

Pure Mg_2Si films have been prepared by pulsed laser deposition (PLD), at 250 °C and 100 mtorr Ar backpressure, onto polished (0.1 μm) 6 mm-diameter

stainless steel substrates, sitting on a piece of silicon wafer. The target was pressed from Mg_2Si , which in turn was prepared by ball-milling Mg and Si metal powders.¹⁵ An XeCl excimer laser at 300 mJ/pulse at 10 Hz was used for PLD.¹⁶ The distance between the target and the substrate was about 5 cm and the deposition time was varied from 10 to 60 minutes to obtain films of different thickness. A film on Si was practically masked and used for film thickness evaluation, whereas films on stainless steel substrate were reserved for electrochemical measurement. The as prepared films appeared shiny and light blue colored. Film thickness was determined using field emission scanning electron microscope (Jeol 6340 FESEM). Examination of the Si wafer after removal of the SS substrate, the film-coated Si wafer, was broken partly and a piece was tilted in the microscope to see the cross-section by SEM. The structure of the film was characterized by X-ray diffraction (XRD) and Raman spectroscopy. The XRD pattern of the film was measured using an X-ray diffractometer (Siemens D500) with Ni filtered Cu $K\alpha$ radiation at 40 kV and 30 mA, and a scan rate of $1.5^\circ / \text{min}$ from 10 to $70^\circ 2\theta$ with 0.05° steps. Raman spectra were recorded using a Labram Raman microscope, ISA Groupe Horiba at ambient conditions. All Raman spectra were recorded using the 632 nm line of a He-Ne laser at 1 mW. The size of the laser beam spot at the sample was $> \sim 1 \mu\text{m}$. Backscattering optics geometry with double notch filter and a standard CCD detector was used to collect, process and analyze the Raman signal. To get a spectrum of lithiated Mg_2Si films, the film was placed in between glass slides and sealed in the He filled glove box to avoid exposure to air. An X-ray photoelectron spectroscopic (XPS) measurement was carried out to investigate the film surface properties.³⁰ From the preliminary results, it was observed that the film surface was Si-rich ($\sim 180\%$) and the Mg/Si ratio increased from 0.61/1 to 0.94/1 with 10 minutes Ar sputtering into the film. Further sputtering to reach the expected ratio of 2/1 was not carried out.

Films were studied electrochemically by embedding the 3 mm-thick disk into the end of a Kel-F rod which was inserted into a polypropylene cell fitted with lithium reference and counter electrode foils and filled with about 5 ml of 1M $\text{LiPF}_6/\text{EC}+\text{DMC}$ (1:1) electrolyte (EM Industries).²¹⁻²³ All the cell assembly and electrochemical characterization were carried out in He filled glove box. Cyclic voltammetry (CV) was carried out at sweep rates from 0.05 to 2.5 mV/s with an EG&G 273 Potentiostat. Films were cycled at a constant current of $35 \mu\text{A}/\text{cm}^2$ between 0.1 and 1.0 V vs Li using an Arbin Battery Cycler (College Station, TX). A single set of Si metal films was prepared by PLD as an electrochemical reference for comparison with Mg_2Si films. The surface images of Mg_2Si film before and after electrochemistry were obtained using atomic force microscope (AFM, Picoscan by Molecular Imaging), operating in contact mode with Si_3N_4 cantilever (cantilever force constant = 0.05 N/m).

Results and Discussion

Film Characterization

Film thickness was measured by SEM cross section image as shown in Figure 1 for the thinnest and thickest films. These results are summarized in Table 1. Most of the films were amorphous to X-ray diffraction. Only the 380 nm film exhibited some crystalline texture, as shown in Figure 2. Comparison of the reflections for Mg_2Si powders used for the target with weak ones in the film indicated a crystal growth of Mg_2Si on the substrate surface,¹³⁻¹⁵ despite of two strong overlapping peaks marked as S at $\sim 43^\circ$ and $\sim 52^\circ$ 2θ of stainless steel substrate.

Raman spectroscopy was used to gain structural information for the film. The vibrational spectrum is a superposition of the spectra of all local structures attributed to the short-range environment around atoms providing more exact structural information without long-range periodicity, in contrast to diffraction data, which give a weighted average of similar interplanar spacings. Figure 3 shows the Raman spectra for the Mg_2Si target, 137 nm PLD film and a Si wafer. Note that Mg_2Si has a cubic structure with the lattice symmetry of $Fm\bar{3}m$, predicting A_{1g} , E_g , F_{2g} Raman active vibration modes.³¹⁻³³ Very strong F_{2g} and weak A_{1g} bands appear in the target but the E_g band is negligible in this material. It has been reported that the F_{2g} band will predominate or become weaker depending on the position where the laser is focused on the Mg_2Si single crystal.^{32,33} Preferred film orientation could be inferred from the data in Fig. 3 from the selectively dominant vibration modes. However, taking into account the XRD data and the ambiguous spectral features of the film, the missing F_{2g} band in this film is probably due to the amorphous nature of the film. Additionally, it was found that the Mg_2Si film had no isolated crystalline Si phase. In contrast to these results, the $\text{Li}_x\text{Mg}_2\text{Si}$ film after electrochemistry exhibits no Raman bands but huge fluorescence bands around 100 cm^{-1} attributed to the presence of lithium salts at the surface.

Cyclic voltammetry of films

The first lithium insertion into the film was done with slow-sweep CV and the third cycles of each film are compared in Figure 4(a). The poor peak definition is characteristic of porous and/or resistive films. The coulombic efficiencies of the first cycle were measured by integrating the anodic and cathodic portions of these curves. Peak intensity increased in proportion to film thickness revealing a good linear accordance with a capacity increase, and suggesting good utilization and a consistency with film density. However, the first cycle losses also increased with film thickness, indicating higher reversibility in thinner film. The enhanced

potential difference between anodic and cathodic peaks with film thickness defines also increased kinetic polarization and internal resistance. There have been a few proposed reaction mechanisms between lithium and Mg_2Si .¹¹⁻¹⁵ Moriga et al¹⁴ and Roberts et al¹⁵ reported that the ternary phase, Li_2MgSi , forms followed by Li-Mg and Li-Si alloys during lithium insertion into the Mg_2Si . The Li-Mg alloy forms at low potential around 0.1 V and Li-Si alloy forms at the potential higher than 0.4 V.¹³⁻¹⁵ Based on the information, the CVs in Figure 4 could be interpreted that significant lithium insertion occurred at low potential, < 0.2 V, and phase changed from Li_2MgSi to Mg_2Si during lithium discharge and Li-Mg and Li-Si dealloyed exhibiting two broad anodic peaks at around 0.3 V and 0.6 V, respectively. A cathodic curve of CV for a Si metal film is also compared in the Figure 4(a). The Si metal film appeared as a rough surface with many irregularly sized grain islands ranging from 0.2 to 1.3 μm . Cathodic peaks at ~ 0.2 , 0.35 and 0.75 V for lithium insertion into the Si metal film indicates that Si follows the similar behavior with that of Mg_2Si film due to alloying of Li with Si. No further anodic or cathodic peaks were observed after the first charge to 0.1 V. Those grains must be damaged so that they are no longer electrochemically active.

As seen in Figure 4(b), the positions of the CV peaks for the films were quite consistent with cycling except for a small cathodic peak at 0.2 V in the first cycle disappeared in the second and third cycles. This behavior seems to be associated with formation of solid electrolyte interface (SEI) layer on the electrode surface during cycling as has been reported for graphite and the SnO electrode.³⁴⁻³⁷ The first cycle of the 137 nm film showed 18.3 % overcharge followed by 14.2 and 11.2 % becoming more stable on cycling.

Potential sweep voltammetry has been used to examine the kinetics of electrochemical processes. Cyclic voltammograms presented as pseudocapacitances of the 137 nm film of Mg_2Si recorded at a sweep rates from 0.1 to 2 mV/s are shown in Figure 5. An increase of sweep rate is correlated with not only a shift of the anodic peaks to higher potential but also enhanced peak height. The morphology and porosity of the film are rate-limiting factors, as a low sweep rate allows cycling in the bulk of the film, in contrast to only film surface participation at high sweep rate. For the higher sweep rate (> 0.5 mV/s), the reaction zone is limited to a small thickness on the surface of the film and the broad anodic peak at ~ 0.6 V partially attributed to dealloying of Li-Si dominate. This is consistent with a Si-rich surface as discussed above and more effective Li-Si surface alloying-dealloying at the surface rather than deep lithium insertion producing Li-Mg alloy. The change of peak shape with sweep rate reflects the kinetics of the lithium reaction at the electrode/electrolyte interface and/or the rate of lithium diffusion in the film. The dependence of height (I_p) of the anodic peak at ~ 0.25 V on sweep rates (v) is shown to be linear with the square-root of the sweep rate in Figure 5. For a kinetically-controlled surface reaction, peak current is

proportional to v , which is typical of the equilibrium behavior of an intercalation electrode. The half-order dependence shown in Fig. 5 suggested that the reaction process in our films is diffusion-controlled. Since the lithium diffusivity in the electrolyte is on the order of $10^{-6} \text{ cm}^2/\text{s}$, we expect solid-state diffusion to dominate in our films. Much slower sweep rates than those used in the present work would be required to gain more information regarding the kinetics.

From the slope of peak current vs $v^{1/2}$, we calculated a chemical diffusion coefficient assuming semi-infinite lithium diffusion.³⁸⁻⁴⁰ For this calculation we assume that the reaction corresponding to the peak current is the removal of one Li^+ from Li_2MgSi , and for lack of other information, we assume that the molar volume of the film is equal to that of the pure Mg_2Si . The calculated diffusivities are quite low, decreasing from 14 to $5.0 \times 10^{-15} \text{ cm}^2/\text{s}$ with increased film thickness as summarized in Table 1. The molar volume of the films could be significantly higher than that of crystalline Mg_2Si and the diffusivities in Table 1 are probably too low. However, the reaction is sluggish compared with that observed with similarly-prepared LiMn_2O_4 .²² Slower lithium diffusion/insertion process for the thicker film suggests that the morphology and/or density of the films changes with thickness.

Constant current cycling

After CV analysis, films were cycled galvanostatically to observe capacity performance during cycling. Figure 6 shows the initial charge-discharge profiles of the films at a constant current density of $35 \mu\text{A}/\text{cm}^2$. Two plateaus at 0.25 and 0.65 V were observed in our films as reported for the Mg_2Si powder electrode.¹¹⁻¹⁵ The initial capacities of the films have no linear correlation with film thickness, due to different rates of surface reaction and diffusion of lithium. However, this changes when the maximum capacities are compared, as seen below.

Figure 7 shows the results of charge-discharge cycling at a current density of $35 \mu\text{A}/\text{cm}^2$. Capacity normalized to electrode area shown in Figure 7(a) increased with increased film thickness. The specific capacity was calculated based on film thickness, electrode area (0.283 cm^2) and the theoretical density ($1.99 \text{ g}/\text{cm}^3$) of Mg_2Si . The cyclability of the thin films was excellent. The thinner films (30 and 137 nm) showed stable capacities greater than 2200 and 890 mAh/g respectively, while thicker films (296 and 380 nm) showed a stabilized capacity $> 790 \text{ mAh/g}$ with some fade after 50 cycles, as seen in Figure 7(b).

In particular, the excellent cycling stability of the 30 nm film electrode, in contrast to the remarkable rapid capacity fade for our thick films and reported for powder electrode,¹¹⁻¹⁵ is noteworthy. The discharge capacity of 2240 mAh/g for the 30 nm film corresponds to 6.4 Li per Mg_2Si . Even though Kim et al has reported the large initial capacity of 1370 mAh/g for Mg_2Si powder corresponding to 3.9 Li per Mg_2Si ,¹³ our value is still exceeds the value of stoichiometric Li-insertion

mechanism. There can be an error from the usage of the theoretical density of Mg_2Si or film thickness evaluation used for gravimetric capacity calculation. Regardless of accepting 10 ~ 20 % errors in the specific capacity calculation, the capacity is still so large that other possible explanations are necessary. As in the previous proposed reaction mechanisms,¹¹⁻¹⁵ lithium insertion into the Mg_2Si matrix together with alloying-dealloying of Li-Si and Li-Mg should be considered to occur in our thin film. Taking account of the noncrystalline and nanometer scale character of our thin film, an extra surface reaction such as lithium adsorption-desorption can be postulated. This surface reaction will be more significant in the thinner films due to the larger surface/volume ratio. Recently Li et al reported that Si metal has a theoretical capacity of 4000 mAh/g or 4.4 Li/Si and their nano-sized Si metal powders delivered 2775 and 2097 mAh/g at the first and second cycles followed by a good capacity retention at > 1700 mAh/g at 0 ~ 0.8 V.²⁷ In this regard, Si richness on our film surface detected by XPS analysis allows us to suggest that Li-Si alloying and dealloying via lithium adsorption and desorption at the Si-rich surface contributes to the large capacity shown by the 30 nm film and probably, a lesser degree to the thicker films.

Lithium diffusion into the thicker film might be slower on initial cycling due to their longer diffusion path to the bulk than that for thinner films. However the initial increase in capacity with cycling and lasting over 50 cycles for the thickest film (380 nm) could be due to an increase in \bar{X}_{Li} with residual Li content in the film. Factors such as volume expansion and weak contact between the very surface and bulk part of film may also affect to the fading of capacity during longer cycling of a thick film.

The plot of dQ/dV normalized to the electrode area (Figure 8) shows clearly that thick film is disadvantageous in the lithium diffusion. The 30 nm film represents the same run almost over all the cycles, while capacity loss is visibly greater as the film becomes thicker. In particular, gaining quite larger capacity in the 50th cycle of the 380 nm film than that in the initial cycle indicates a slower lithium diffusion to the thick film due to long diffusion path. In this context, thinner films on nanometer scale are obviously favored for more stable cycling and higher coulombic efficiency, which is consistent with the CV analysis results.

Self-discharge reaction

Self-discharge reaction is apparent for these films. When the film is allowed to relax after charging to 0.1 V, the potential tends to increase very slowly to near 1.0 V. It is thus suggested that side reaction with the electrolyte or a transformation of original Mg_2Si cubic phase to another one by lithiation may be responsible for the low initial coulombic efficiency of films shown in Figure 7(c). The coulombic efficiency is even worse for constant current cycling than for CV. However, increasing efficiency and decreasing deviation of the IR drop with cycle number

suggests a slowing in the side-reaction with the build-up of the SEI layer and the stabilization of $\text{Li}_x\text{Mg}_2\text{Si}$ phase. The chemistry of the SEI layer was preliminarily examined using X-ray photoelectron and reflectance FTIR spectroscopy on 137 nm $\text{Li}_x\text{Mg}_2\text{Si}$ film obtained after electrochemistry. The analysis results of the spectra indicated that the SEI layer is composed of LiF, Li_2CO_3 salts and lithium alkyl carbonates such as ROCO_2Li formed by electrolyte decomposition. Normally the electrolyte decomposition reaction occurs below 1.2 V vs Li, where our films are operated. Possible self-desorption of Li atoms from the surface of particularly the 30 nm film may contribute to the self-discharge reaction.

Film morphology change

AFM was used to examine the film morphology before and after electrochemical cycling. AFM surface images (Figure 9) indicate that small grains (≥ 50 nm) cover a rough surface (76 Å roughness) of stainless steel substrate, reducing the surface roughness considerably to 17 Å. However, the surface morphology of the film has been substantially modified after cycling. The roughness of the film increased 24 times after electrochemistry (407 Å). Small grains are still observed in the film but most of them seem to be agglomerated or coated by a SEI layer. Electrochemical agglomeration has been observed on nano-sized active alloy powders with particle sizes less than 100 nm, even if cracking or crumbling accompanied by severe crystal structural changes occurred by lattice volume expansion-contraction have been normally observed during cycling of powder intermetallic anodes with larger particle size.⁵⁻¹⁵ It has been reported that nano-sized Si, SnSb, etc. anodes exhibit similar aggregation on Li-insertion for which the metal elements can react with Li ions to form an alloy.^{20,27,28} Though the agglomeration was observed in this work, it is surprising to see continuous stable cycling as observed in Figure 7 and 8. However, as film thickness increases, the aggregation together with SEI layer formation will lead to increase the diffusion length.

The stable behavior observed with the thin film electrodes in this study, even in the presence of agglomeration with cycling, may be due to their poor crystallinity accompanied by a surface lithium adsorption and reversible Li-Si alloying. In addition to the general geometrical (2-dimnesion) advantage of thin films, PLD films have a particularly strong physical adherence to the substrate. This may inhibit volume change in the particles and improve the conductivity of these electrodes. Based on our experimental findings, we propose that preparation of amorphous nanometer scaled thin film and/or well dispersed intermetallics anode particles can help to improve their electrochemical performance for rechargeable lithium batteries.

Conclusion

Thin PLD films of nanocrystalline amorphous Mg_2Si showed stable cycling behavior between 0.1 and 1.0 V vs Li, yielding a reversible capacity as great as 2200 mAh/g for 30 nm film. However, the thicker films showed fade rates of about 0.5 ~ 0.6 %/cycle, out to 140 cycles. The stability of the thinner film of 30 nm seems to originate from more amorphous character, reversible lithium surface adsorption and desorption forming Li-Si alloy at the surface/SEI layer, shorter diffusion paths, reduced lattice volume change due to 2-dimensional nature of thin film and build-up of stable SEI layer at the initial charge-discharge.

Acknowledgments

We would like to thank R. Kostecki for the AFM and Raman measurements and helpful discussion. We are grateful to National Center for Electron Microscopy (NCEM) of Lawrence Berkeley National Laboratory for FESEM images. SWS would like to thank Prof. M. Yoshimura in Tokyo Institute of Technology for his continuous encouragement. This work was supported by the Office of Energy Research, Basic Energy Sciences, Chemical Sciences Division of the Department of Energy under contract No. DE-ACO3-76SF00098.

References

1. M. M. Thackeray, J. O. Thomas and M. S. Whittingham, *MRS Bulletin*, **3**, 39 (2000).
2. B. A. Boukamp, G. C. Lesh and R. A. Huggins, *J. Electrochem. Soc.*, **128**, 725 (1981).
3. J. Wang, I. D. Raistick and R. A. Huggins, *J. Electrochem. Soc.*, **133**, 457 (1986).
4. M. Winter, J. O. Besenhard, M. E. Spahr and P. Novak, *Adv. Mater.*, **10**, 725 (1998).
5. K. D. Kepler, J. T. Vaughey and M. M. Thackeray, *Electrochem. Solid-State Lett.*, **2**, 307 (1999).
6. O. Mao and J. R. Dahn, *J. Electrochem. Soc.*, **146**, 423 (1999).
7. H. Sakaguchi, H. Honda and T. Esaka, *J. Power Sources*, **81-82**, 229 (1999).
8. J. Yang, Y. Takeda, N. Imanishi, T. Ichikawa and O. Yamamoto, *Solid State Ionics*, **135**, 175 (2000).
9. J. T. Vaughey, J. O' Hara and M. M. Thackeray, *Electrochem. Solid-State Lett.*, **3**, 13 (2000).
10. H. Kim, Y. J. Kim, D. G. Kim, H. J. Sohn and T. Kang, *Solid State Ionics*, **144**, 41 (2001).
11. R. A. Huggins and A. A. Anani, US Patent 4,950,566 (1990).
12. A. A. Anani and R. A. Huggins, *J. Power Sources*, **38**, 363 (1992).
13. H. Kim, J. Choi, H. J. Sohn and T. Kang, *J. Electrochem. Soc.*, **146**, 4401 (1999).
14. T. Moriga, K. Watanabe, D. Tsuji, S. Massaki and I. Nakabayashi, *J. Solid State Chem.*, **153**, 386 (2000).
15. G. A. Roberts, E. J. Cairns and J. A. Reimer, *J. Power Sources*, in press (2002).
16. S. W. Song, K. A. Striebel and E. J. Cairns, in *Batteries*, submitted, The Electrochemical Society Proceedings Series, San Francisco, CA (2001).
17. J. O. Besenhard, J. Yang and M. Winter, *J. Power Sources*, **68**, 87 (1997).
18. D. Larcher, L. Y. Beaulieu, D. D. MacNeil and J. R. Dahn, *J. Electrochem. Soc.*, **147**, 1658 (2000).
19. Y. Xia, T. Sakai, T. Fujida, M. Wada and H. Yoshinaga, *J. Electrochem. Soc.*, **148**, A471 (2001).
20. H. Li, L. Shi, W. Lu, X. Huang and L. Chen, *J. Electrochem. Soc.*, **148**, A915 (2001).
21. K. A. Striebel, C. Z. Deng, S. J. Wen and E. J. Cairns, *J. Electrochem. Soc.*, **143**, 1821 (1996).
22. A. Rougier, K. A. Striebel, S. J. Wen and E. J. Cairns, *J. Electrochem. Soc.*, **145**, 2975 (1998).

23. A. Rougier, K. A. Striebel, S. J. Wen, T. J. Richardson, R. P. Reade and E. J. Cairns, *Appl. Surf. Sci.*, **134**, 107 (1998).
24. T. Brousse, R. Retoux, U. Herterich and D. M. Schleich, *J. Electrochem. Soc.*, **145**, 1 (1998).
25. S. C. Nam, Y. H. Kim, W. I. Cho, B. W. Cho, H. S. Chun and K. S. Yun, *Electrochem. Solid State Lett.*, **2**, 9 (1999).
26. J. Yang, Y. Takeda, N. Imanish and O. Yamamoto, *J. Electrochem. Soc.*, **146**, 4009 (1999).
27. H. Li, X. Huang, L. Chen, Z. Wu and Y. Liang, *Electrochem. Solid State Lett.*, **2**, 547 (1999).
28. N. Li, C. R. Martin and B. Scrosati, *Electrochem. Solid State Lett.*, **3**, 316 (1999).
29. S. Grungeon, S. Laruelle, R. Herrera-Urbina, L. Dupont, P. Poizot and J. M. Tarascon, *J. Electrochem. Soc.*, **148**, A285 (2001).
30. X. Zhang, C. Lee and P. N. Ross, Jr., Abstracts of Joint International Meeting of The 200th Electrochemical Society and The 52nd International Society of Electrochemistry, No. 233, San Francisco, CA (2001).
31. W. G. Fately, *Infrared and Raman Selection Rules for Molecular and Lattice Vibrations: The Correlation Method*, Wiley-Interscience, New-York (1972).
32. C. J. Buchenauer and M. Cardona, *Phys. Rev. B*, **3**, 2504 (1971).
33. S. Onari and M. Cardona, *Phys. Rev. B*, **14**, 3520 (1976).
34. D. Aurbach, Y. Ein-Eli, O. Chusid, Y. Carmeli, M. Babai and H. Yamin, *J. Electrochem. Soc.*, **141**, 603 (1994).
35. R. Imhof and P. Novak, *J. Electrochem. Soc.*, **145**, 1081 (1998).
36. S. K. Jeong, M. Inaba, T. Abe and Z. Ogumi, *J. Electrochem. Soc.*, **148**, A989 (2001).
37. H. Li, X. Huang and L. Chen, *Electrochem. Solid State Lett.*, **1**, 241 (1998).
38. M. D. Levi and D. Aurbach, *J. Electroanal. Chem.*, **421**, 79 (1997).
39. M. D. Levi and D. Aurbach, *Electrochim. Acta*, **45**, 167 (1999).
40. A. J. Bard and L. R. Faulkner, *Electrochemical Methods; Fundamentals and Applications*, John Wiley & Sons, New-York (1980).

Table 1. Electrochemical properties of Mg₂Si films with different film thickness.

PLD time (min)	Thickness (nm)	Discharge capacity ($\mu\text{Ah}/\text{cm}^2$) ^a	Volumetric capacity ($\mu\text{Ah}/\text{cm}^2 \cdot \mu\text{m}$) ^a	Specific capacity (mAh/g) ^a	Coulombic efficiency ^a	Chemical diffusion coefficient, \check{D}_{Li} (cm^2/s)
10	30	13.4	446	2241	0.94	1.4×10^{-14}
20	137	24.3	178	893	0.83	1.4×10^{-14}
40	296	47.1	159	799	0.89	1.3×10^{-14}
60	380	61.0	161	807	0.89	5.0×10^{-15}

^a These are maximum values.

Figure captions

Figure 1. Scanning electron microscopic images of Mg_2Si films; film thickness is (a) 30 nm and (b) 380 nm.

Figure 2. X-ray diffraction patterns of (a) Mg_2Si powder used for the target and (b) 380 nm Mg_2Si PLD film; * unknown peak.

Figure 3. Micro-Raman spectra of (a) Mg_2Si target, (b) 137 nm Mg_2Si PLD film and (c) Si wafer excited at 632 nm by He-Ne laser; ■ overtone.

Figure 4. Comparative cyclic voltammograms of (a) Mg_2Si films with various film thickness of 30, 137, 296 and 380 nm and a cathodic curve of Si metal film in 1 M $\text{LiPF}_6/\text{EC}+\text{DMC}$ and of (b) 137 nm thick film on continuous three cycles; at sweep rate = 0.1 mV/s.

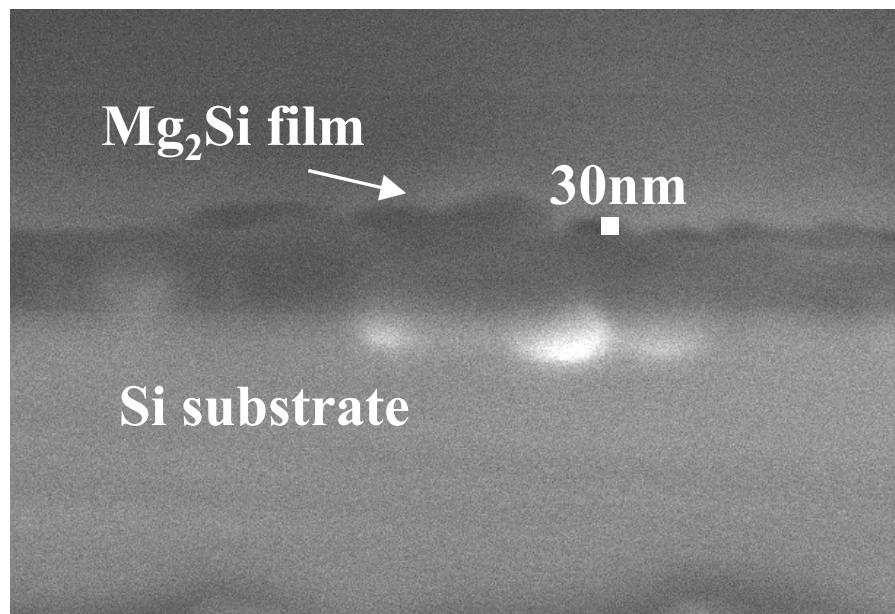
Figure 5. Cyclic voltammograms (a) of 137 nm Mg_2Si film at sweep rates from 0.1 to 2.5 mV/s, and plots of (b) I_p vs v and (c) I_p vs \sqrt{v} .

Figure 6. Voltage profiles of the Li/ Mg_2Si cells for the (a) 30, (b) 137, (c) 296 and (d) 380 nm thick films as a function of time.

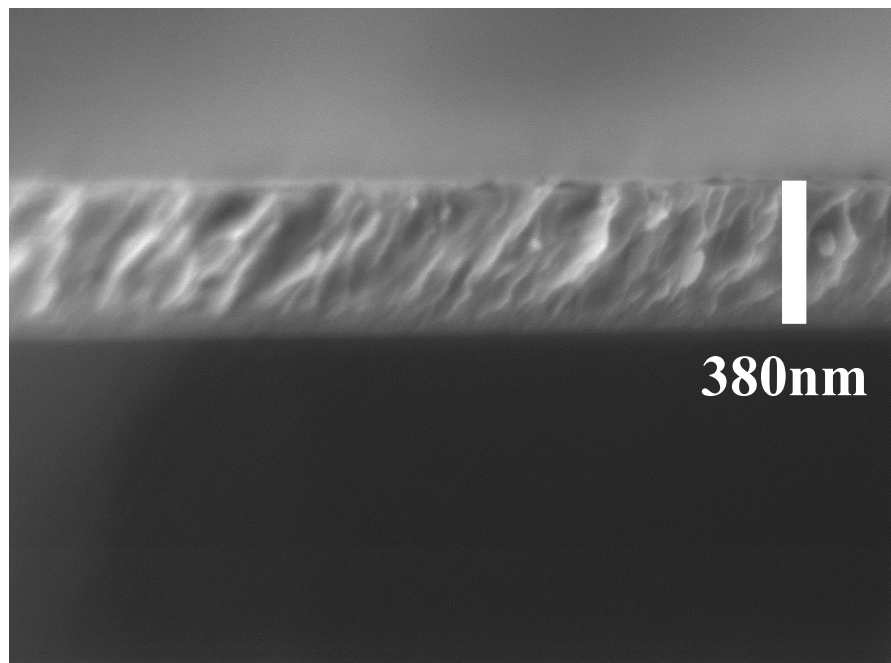
Figure 7. Comparative plot of (a) observed discharge capacity normalized electrode area, (b) calculated specific discharge capacity and (c) coulombic efficiency with cycle number for 30 (-□-), 137(-◊-), 296 (-●-) and 380 nm (-◇-) Mg_2Si films, obtained by cycling at a constant current density of $35 \mu\text{A}/\text{cm}^2$ in 1 M $\text{LiPF}_6/\text{EC}+\text{DMC}$.

Figure 8. Plots of dQ/dV vs V of the (a) 30, (b) 137, (c) 296, and (d) 380 nm Mg_2Si films at different cycle numbers.

Figure 9. Film surface morphology observed by AFM for (a) stainless steel substrate and 137 nm Mg_2Si film (b) before and (c) after cycling.



(a)



(b)

Figure 1.

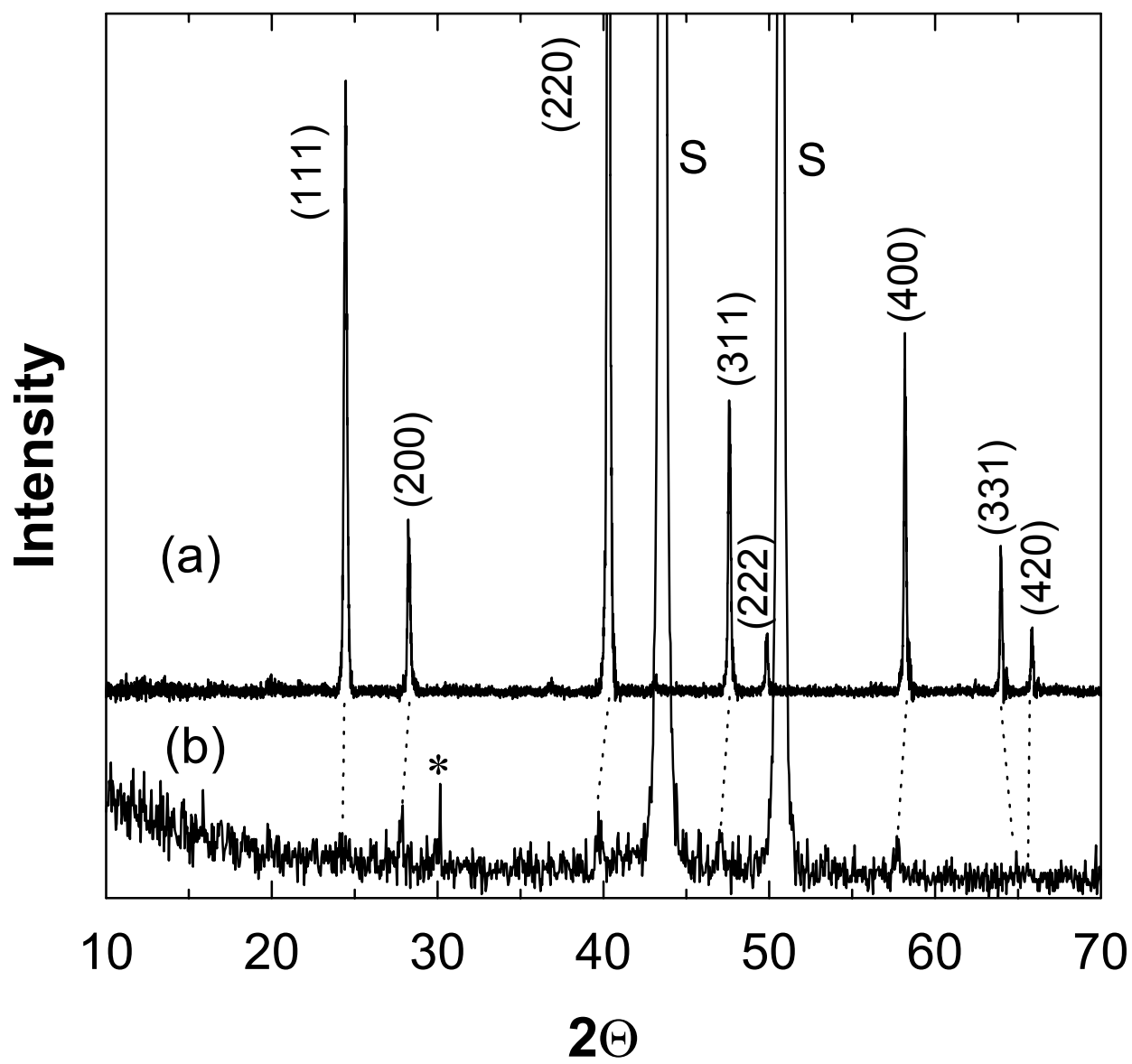


Figure 2.

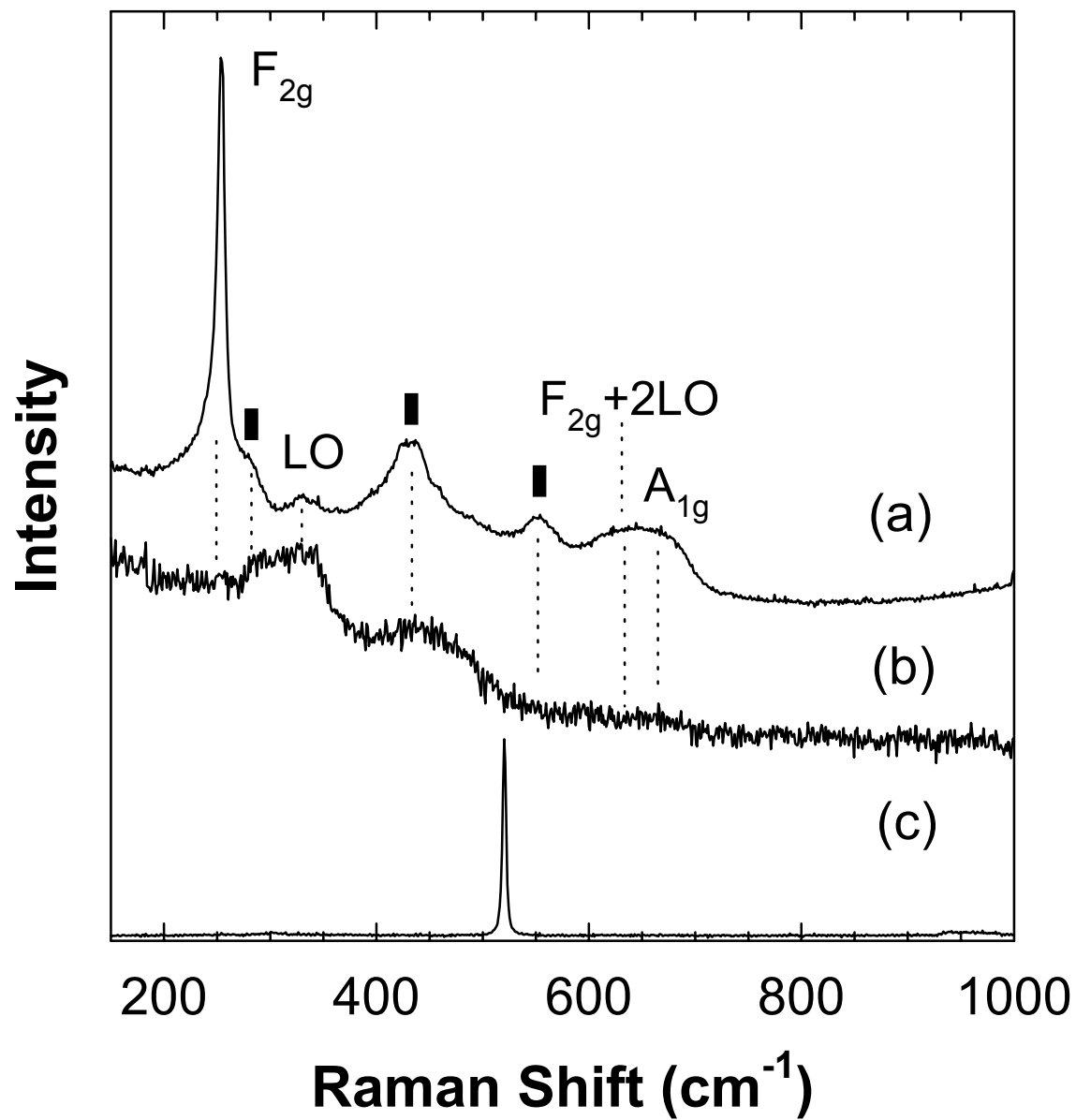


Figure 3.

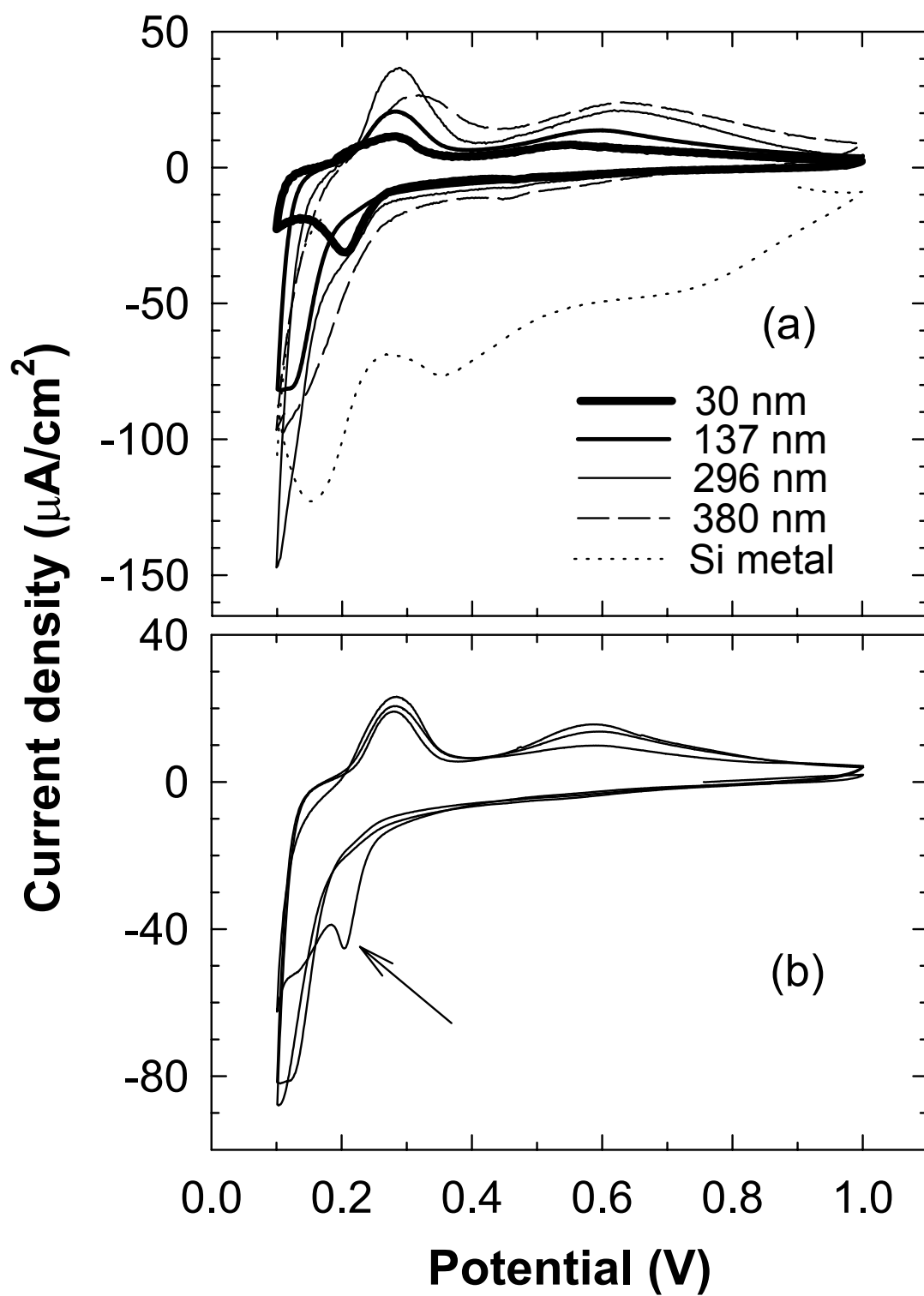


Figure 4.

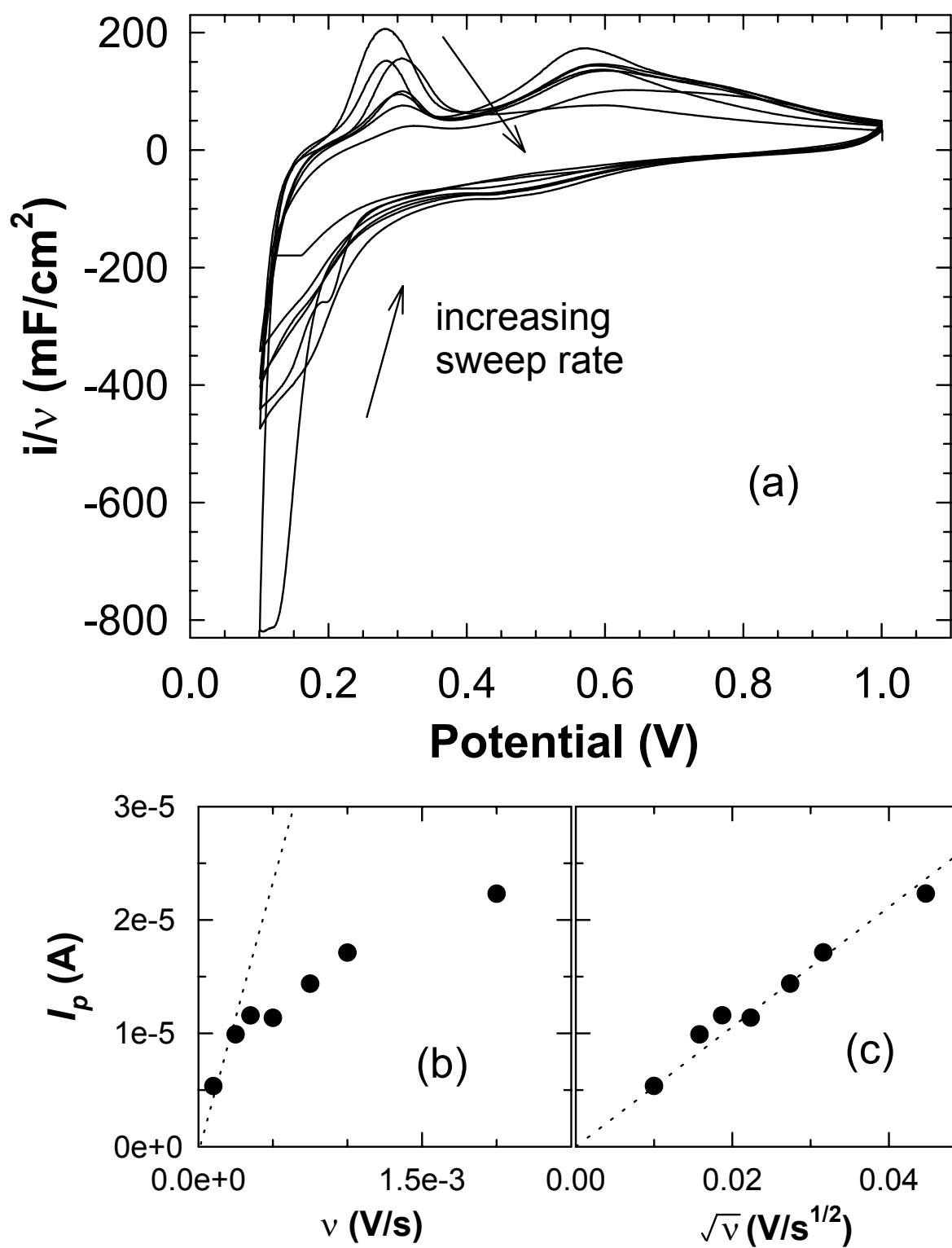


Figure 5

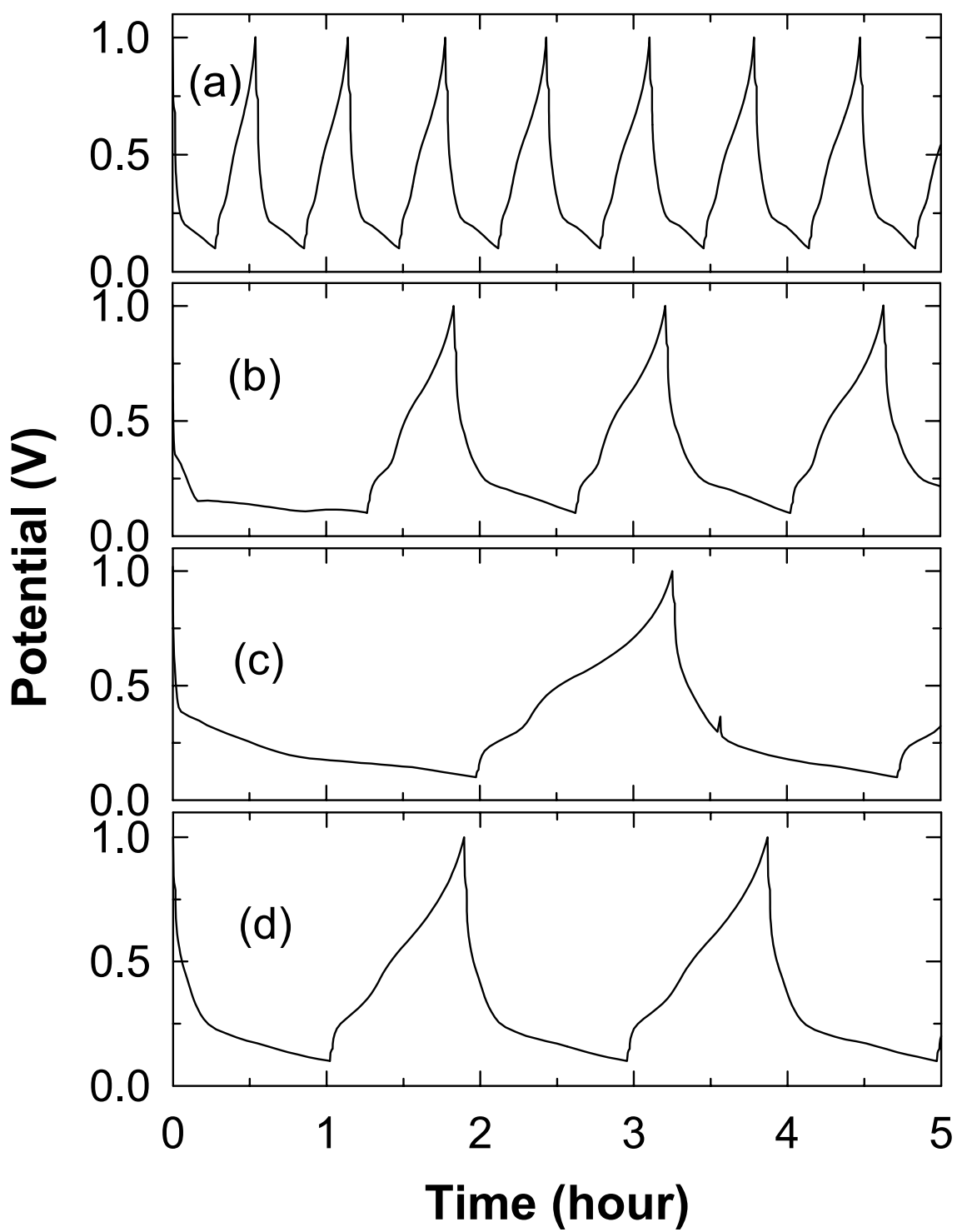


Figure 6

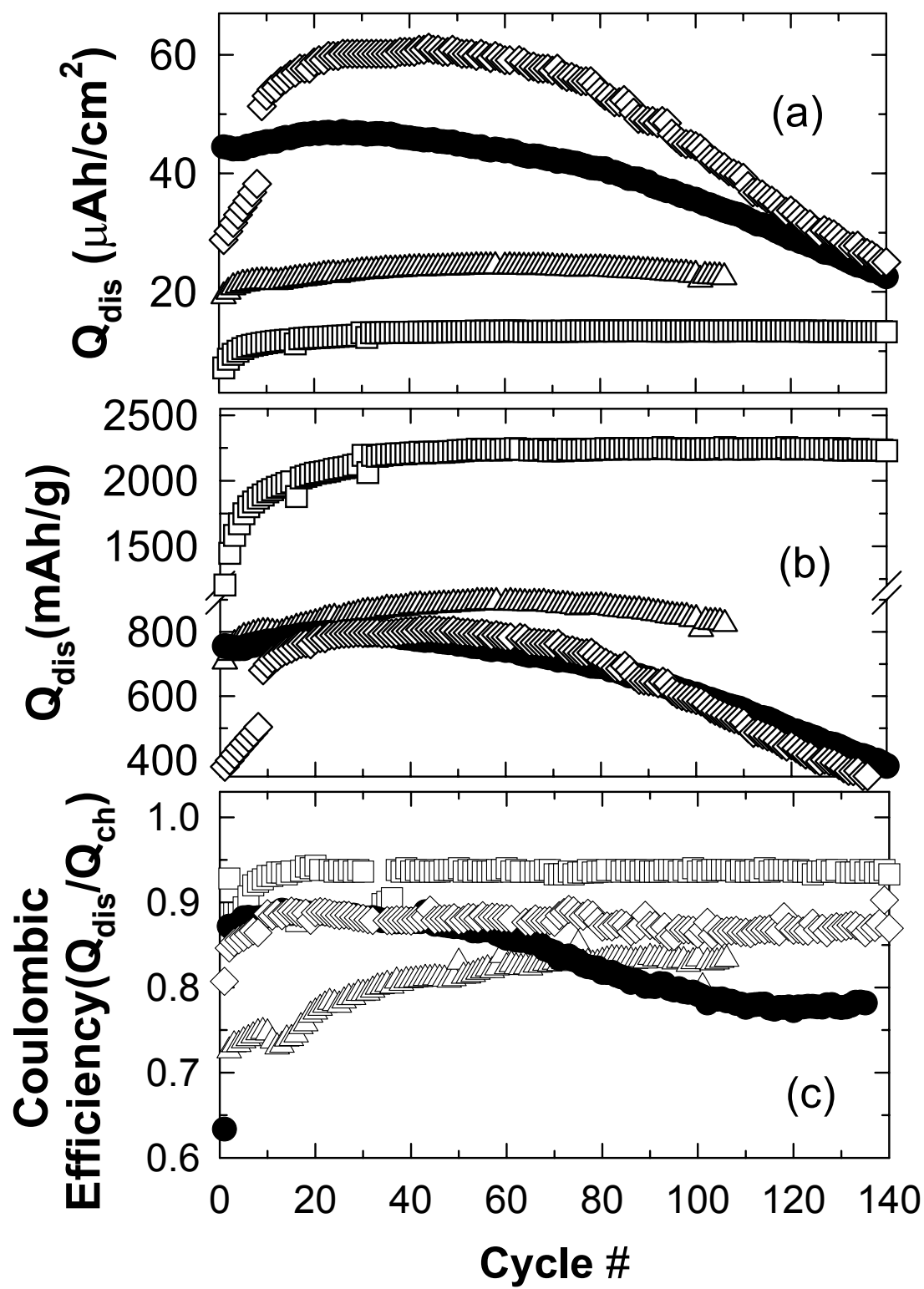


Figure 7

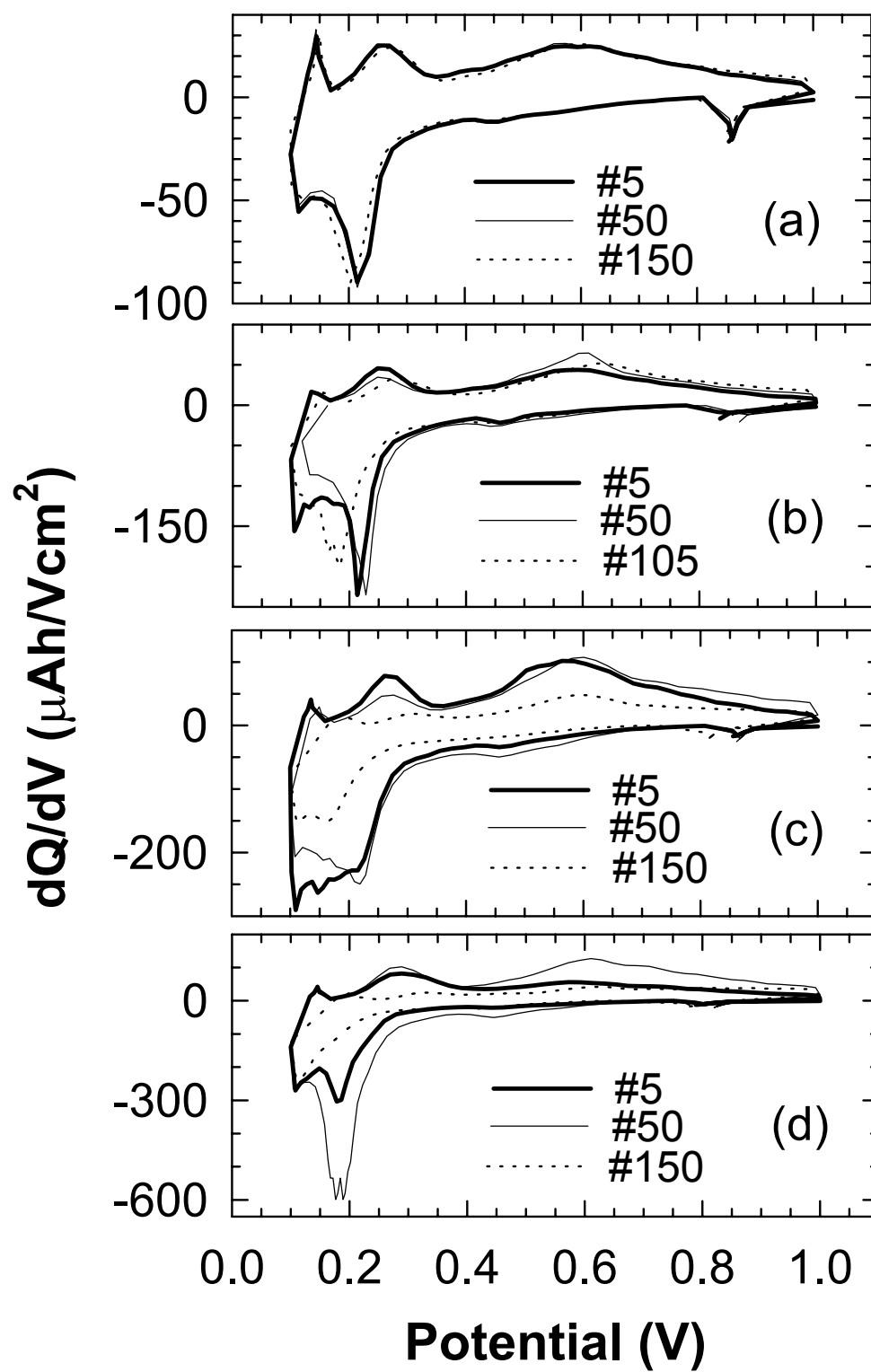


Figure 8

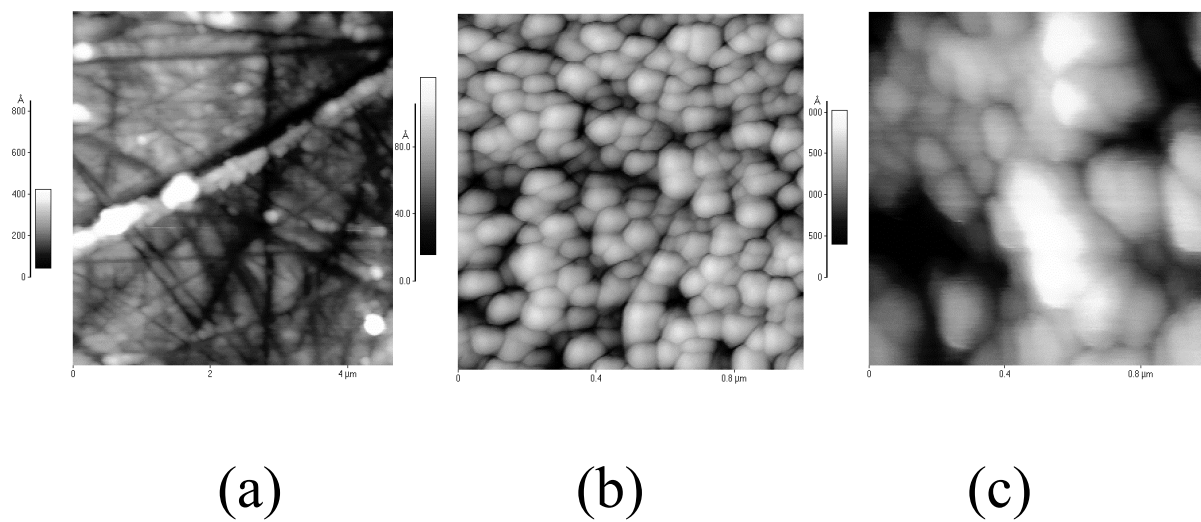


Figure 9